

# Enhanced Second-Harmonic Generation of van der Waals $\text{CuInP}_2\text{S}_6$ via Pressure-Regulated Cationic Displacement

Kejun Bu,<sup>||</sup> Tonghuan Fu,<sup>||</sup> Ziwan Du, Xin Feng, Dong Wang, Zhongyang Li, Songhao Guo, Zongdong Sun, Hui Luo, Gang Liu, Yang Ding, Tianyou Zhai, Qian Li, and Xujie Lü\*



Cite This: <https://doi.org/10.1021/acs.chemmater.2c03066>



Read Online

ACCESS |



Metrics & More

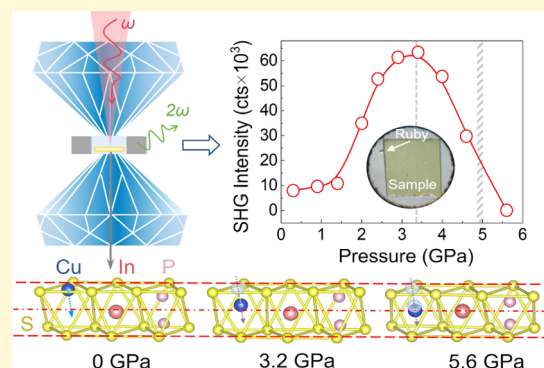


Article Recommendations



Supporting Information

**ABSTRACT:** Design and exploration of high-performance nonlinear optical (NLO) materials have long been sought with the goal of tunable local structures and NLO properties for advanced laser technology. Thus far, the design strategies for second-order NLO materials have been mainly focused on anionic groups that have made great progress in the development of new NLO compounds. However, few studies have focused on the effects of cationic components and their contributions to NLO properties have long been underappreciated and remain unclear. Here, by introducing pressure to continuously tune the Cu displacement, we demonstrate the significant role of the cationic configuration in NLO properties, and a remarkable enhancement by one order of magnitude in second-harmonic generation (SHG) has been achieved at 3.4 GPa in thiophosphate  $\text{CuInP}_2\text{S}_6$  (CIPS). *In situ* high-pressure structural characterization indicates that Cu cations move from the van der Waals edge to the cages of  $\text{S}_6$  octahedra during compression and subsequently form highly distorted  $[\text{CuS}_6]$  octahedra at 3.2 GPa. We quantitatively demonstrate the contributions of cationic displacement on the octahedral distortion and interband dipole moments, which dominate optical nonlinearity and determine the enhanced SHG. This work deepens the fundamental understanding of the relationship between cationic displacement and SHG properties, thus providing new paths to NLO material design by optimizing the cationic configurations.



## INTRODUCTION

Nonlinear optical (NLO) materials are of great importance in laser science and optical communications owing to their capability to convert light energy and produce coherent sources.<sup>1–4</sup> Over the past few decades, enormous efforts have been made to improve second-order NLO properties by increasing the nonlinear polarizability of NLO-active anionic groups.<sup>5,6</sup> The structural characteristics of these NLO-active units have been revealed to be noncentrosymmetric and locally distorted, which contribute to high second-harmonic generation (SHG).<sup>7,8</sup> Following these clues, many design strategies based on anionic groups have been developed, such as increasing off-centering distortion in anionic octahedra,<sup>9,10</sup> introducing planar  $\pi$ -conjugated or distorted tetrahedral anionic group,<sup>11,12</sup> and partially substituting isovalent anions.<sup>13,14</sup> However, the structural design and optimization of cationic moieties have long been ignored and the role of cation modification is underappreciated, which limit the further development of high-performance NLO materials. To this end, suitable material systems are needed in combination with effective regulation and advanced *in situ* characterization methods.

Noncentrosymmetric layered thiophosphates (LTPs), with tunable two-dimensional (2D) structures, are promising

candidates for SHG applications.<sup>15–17</sup> The relatively low oxidation states of metal cations in the rigid  $[\text{P}_2\text{S}_6]^{4-}$  framework usually exhibit off-centering distortion, which is responsible for the microscopic second-order nonlinear susceptibility.<sup>15</sup> Remarkably, the cationic positions can vary in a certain range without changing the overall structures in LTPs, making it possible to finely tune the local structural distortions.<sup>18–21</sup> Moreover, the van der Waals (vdW) layered structure with weak interlayer bonding gives a higher tunability of polarization and also an additional space for distortion tolerance. Such tunable and flexible structures offer a rare opportunity for regulating and optimizing the cation displacement and thus provide an avenue to achieve enhanced or emergent SHG properties. Alternative to traditional chemical or physical methods such as doping or strain, pressure provides an effective means to adjust atomic interactions meanwhile coupled with *in situ* physical property characterizations.<sup>22–27</sup>

Received: October 7, 2022

Revised: December 5, 2022

Applying high pressure to these LTPs could enable the continuous tuning of their cationic displacement, the degree of local distortion, and the polarization of optically active structural units in a controlled manner.

We select a typical noncentrosymmetric vdW CuInP<sub>2</sub>S<sub>6</sub> (CIPS) as the prototype and introduce pressure to regulate the Cu displacement and the local distortions. A recent study by Lu et al. provides exciting findings by extending strain-induced nanoengineering to enhance the SHG properties of CIPS, which indicates the significant role of local structures in SHG properties.<sup>17</sup> Understanding the relationship between local structures and SHG is thus highly desirable but challenging since the structures of wrinkled nanostructures are hard to be characterized. In this work, using *in situ* high-pressure diagnostics and theoretical simulations, we systematically investigated the relationship between SHG properties and the local configuration of Cu cations. Pressure processing continuously regulates the Cu displacement from the vdW edge to the cage formed by six S atoms and subsequently formed distorted [CuS<sub>6</sub>] octahedra, which causes significant enhancement in SHG response. With the help of first-principles calculations, we elucidate the relationship between the distorted Cu cationic coordination and dipole moments and further reveal the effects on SHG properties.

## EXPERIMENTAL SECTION

**Synthesis.** Copper powder (Aladdin, 99.9%), indium powder (Aladdin, 99.99%), red phosphorus lump (Aladdin, 98.5%), and sulfur powder (Aladdin, 99.95%) were weighed in accordance with a stoichiometric ratio of 1:1:2:6. The raw materials were put together and sealed in a fused quartz tube under high vacuum ( $\sim 10^{-3}$  Pa). The tube was then heated to 600 °C over 12 h and soaked for 10 days in a muffle furnace to fabricate polycrystalline CIPS bulk. High-quality CIPS single-crystal flakes were fabricated by the chemical vapor transport method. The as-synthesized polycrystalline bulk (3 g) and transport agent I<sub>2</sub> (50 mg) were put at the bottom of a tube. The tube was sealed as before, placed, and heated in a two-zone furnace with 680 and 750 °C for 7 days. The bottom of the tube was placed in the hot zone. After the transport process, yellow crystals were obtained in the cold zone.

***In situ* High-Pressure Characterizations.** High-pressure experiments were performed under static pressure conditions with diamond anvil cell (DAC) equipment. Type II-a ultralow fluorescence diamonds were used in the optical experiments. The pressure was determined by the ruby fluorescence method.<sup>28</sup>

**X-ray Crystallography.** The *in situ* powder X-ray diffraction (XRD) at high pressures was carried out at the experimental station 13 BM-C (GSECARS) of Advanced Photon Source (APS), Argonne National Laboratory (ANL). The X-ray beam was monochromated with silicon 311 crystal to 28.6 keV (0.434 Å), with 1 eV bandwidth. A MAR165 charge-coupled device (CCD) detector (Rayonix) was used, and the ambient LaB<sub>6</sub> powder was used to calibrate the distance and tilting of the detector. Silicone oil was used as the pressure-transmitting medium.<sup>29</sup> The diffraction patterns were collected by the MarCCD detector and integrated using Dioptas software.<sup>30</sup> Rietveld analyses of the powder XRD data were performed using Fullprof software.<sup>31</sup> The *in situ* single-crystal XRD (SXRD) at high pressures was carried out at a Bruker D8QUEST diffractometer equipped with Ag K $\alpha$  radiation. Suitable single crystals in DACs were chosen to perform the data collection. Neon was used as the pressure-transmitting medium. The diffraction data were collected at room temperature only by the  $\omega$ -scan method at three fixed  $2\theta$  ( $-20$ ,  $0$ , and  $20^\circ$ ). Eight runs were collected, and an exposure time of 60 s for each diffraction frame was used for higher completeness. The crystal structures were solved and refined using the APEX3 program.<sup>32</sup> Absorption corrections were performed to use the multiscan method (ASDABS). The monoclinic phase around 2 GPa and the trigonal

phase after the phase transition were determined by the SXRD (Table S2). Then, we used the structural information resolved from SXRD results to refine the powder XRD patterns. The fitting of the pressure–cell volume ( $P$ – $V$ ) curve used the third-order Birch–Murnaghan equation of state<sup>33</sup>

$$P(V) = \frac{3B_0}{2} \left[ \left( \frac{V_0}{V} \right)^{7/3} - \left( \frac{V_0}{V} \right)^{5/3} \right] \left\{ 1 + \frac{3}{4}(B' - 4) \left[ \left( \frac{V_0}{V} \right)^{2/3} - 1 \right] \right\} \quad (1)$$

where  $V_0$  is the initial volume,  $V$  is the deformed volume,  $B_0$  is the isothermal bulk modulus with respect to pressure, and  $B'$  is the derivative of the bulk modulus with respect to pressure. The quadratic elongation parameter  $\lambda$  was used to characterize the local structural distortion of octahedra<sup>34</sup>

$$\langle \lambda \rangle = \frac{1}{6} \sum_{i=1}^6 \left( \frac{d_i}{d_0} \right)^2 \quad (2)$$

where  $d_i$  is the Cu–S bond lengths and  $d_0$  is the mean Cu–S bond distance. According to the equation, for an ideal octahedron without distortion,  $\lambda = 1$ .

**UV–vis–NIR Absorption Spectroscopy.** Absorption spectra were collected using a Xeon light source between 300 and 1100 nm. The absorption spectra and optical images were measured in a home-designed spectroscopy system in a microregion (Gora-UVN-FL, built by Ideaoptics). Silicone oil was used as the pressure-transmitting medium. The  $\alpha^2$  vs the  $h\nu$  curve was extrapolated to determine the band gap.<sup>35</sup>

**Raman Spectroscopy.** Raman spectra were measured on a low-wavenumber Renishaw Raman microscope using a 532 nm laser. Neon was used as the pressure-transmitting medium. We also investigated the phonon vibrational anisotropy of CIPS by angle-resolved polarized Raman spectroscopy (ARPRS). The polarization dependence of Raman was measured by sending the linearly polarized excitation beam through a motorized achromatic half-wave plate, and the signal was collected by rotating a motorized linear polarizer. The Raman signal was calculated using the equation  $I \propto |e_i \mathbf{R} e_s|^2$ ,<sup>36,37</sup> where  $e_i$ ,  $e_s$ , and  $\mathbf{R}$  represent the polarization vectors of the incident light, scattered light, and the Raman tensor, respectively.

**Second-Harmonic Generation Measurement.** SHG experiment was measured in a home-designed optical system. A femtosecond laser (NPI LASER Co., Ltd., 1030 nm, 25 MHz, 200 fs) was used as the exciting light source. A 20 $\times$  objective was used to focus the laser with a laser beam of 40  $\mu$ m in diameter. A spectrometer (Nova, Ideaoptics Co., Ltd.) was employed to collect the SHG signal. Silicone oil was used as the pressure-transmitting medium. The polarization-dependent SHG experiment was carried out by linearly polarized light. The generation of the linear polarization was based on rotating a half-wave plate. The linearly polarized light focused on the surface of a high-quality single crystal, and the subsequently excited SHG signal was detected by the spectrometer.

**First-Principles Calculations.** First-principles calculations were performed using the Vienna Ab initio Simulation Package (VASP). The structural relaxations were carried out using generalized gradient approximation (GGA) implemented in the Perdew–Burke–Ernzerhof (PBE) method as the exchange–correlation function until the total energies and forces converge to  $10^{-5}$  eV and 0.01 eV/Å, respectively.<sup>38,39</sup> The cutoff energy of the plane wave was chosen at 450 eV. The  $k$ -point grid of  $8 \times 4 \times 4$  was used for the conventional cell. The high-symmetry points in the Brillouin zones were considered in our band structure calculations. The following paths are  $Y(0\ 1\ 0) - \Gamma(0\ 0\ 0) - A(0.0\ 0.0\ 0.5) - M(0.0\ 1.0\ 0.5) - \Gamma(0\ 0\ 0)$  in the monoclinic phase. Crystal orbital Hamilton population (COHP) calculations were computed using the LMTO package, and the original basis set and its basic functions manage to reconstruct the PAW electronic structure. Calculations of the optical properties

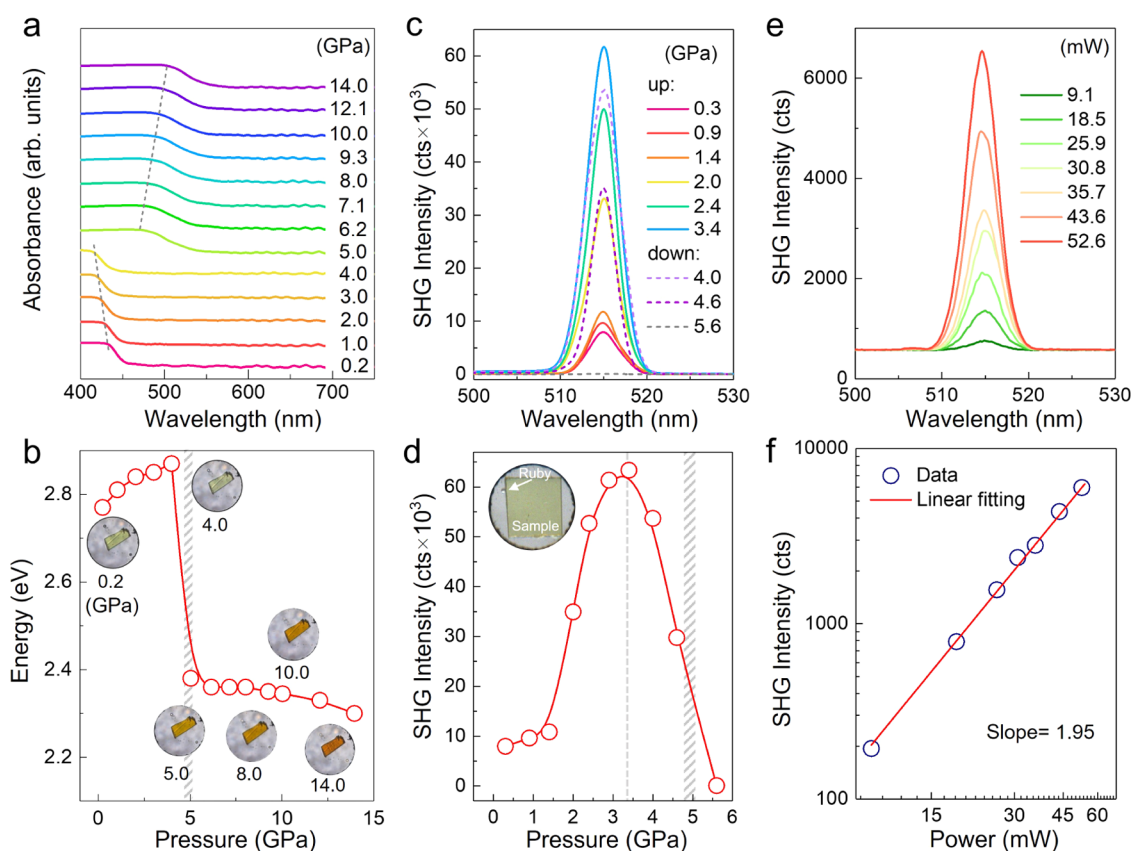


**Figure 1.** Optical and SHG properties of CIPS at different pressures. (a) Selected UV–vis absorption spectra of CIPS single crystal under different pressures. (b) Band gap evolution during compression and the optical images at selected pressures. (c) SHG spectra of CIPS collected at different pressures. (d) SHG intensities as a function of pressure, showing a volcano shape. (e) SHG spectra in the incident light of 1030 nm with different laser power from 9.1 to 52.6 mW. (f) Linear fitting of power-dependent SHG intensities, showing a slope of 1.95.

described in terms of the complex dielectric function  $\epsilon(\omega) = \epsilon^{\text{Re}}(\omega) + i\epsilon^{\text{Im}}(\omega)$  were made, in which  $\epsilon^{\text{Re}}(\omega)$  and  $\epsilon^{\text{Im}}(\omega)$  are the real and imaginary parts of the dielectric function, respectively.<sup>40,41</sup> The first-order nonresonant susceptibility at the low-frequency region is given by  $\chi^{(1)}(\omega) = \epsilon^{\text{Re}}(\omega) - 1$ , and the second-order susceptibility can be expressed in terms of the first-order susceptibilities as follows<sup>42</sup>

$$\chi_{ijk}^{(2)}(\omega_3, \omega_1, \omega_2) = \frac{ma}{N^2 e^3} \chi_{ii}^{(1)}(\omega_3) \chi_{jj}^{(1)}(\omega_1) \chi_{kk}^{(1)}(\omega_2) \quad (3)$$

The  $m$ ,  $e$ , and  $N$  are the electron mass, electron charge, and number density of the atoms, respectively, and the parameter  $a$  represents the nonlinear response.

## RESULTS AND DISCUSSION

**Piezochromism and Pressure-Induced SHG Enhancement.** We first investigated the pressure-induced changes in optical band gap using *in situ* ultraviolet–visible (UV–vis) absorption spectroscopy. CIPS is a yellow crystal with a band gap of 2.78 eV at ambient pressure.<sup>43</sup> During compression, the band gap slightly increases to 2.88 eV from 0 to 4.0 GPa, and then, an abrupt drop with obvious color change occurs at 5 GPa, which is caused by the noncentrosymmetric-to-centrosymmetric structural phase transition (we will elaborate on this later); after the transition, band gap narrows slightly during further compression and decreases to 2.30 eV with dark orange color at 14 GPa (Figure 1a,b). To examine the variations of optical nonlinearity, high-pressure single-crystal SHG measurements under an excitation wavelength of 1030 nm were performed. During compression, a significantly enhanced SHG response is observed, reaching the maximum

at 3.4 GPa, which is 10 times higher than that under ambient conditions (Figure 1c,d). This SHG intensity is comparable to that of  $\text{KH}_2\text{PO}_4$  (KDP) under ambient conditions (Figure S1), which indicates a strong SHG response in CIPS under pressure. The SHG intensity decreases rapidly during further compression, and no signal can be detected over 5 GPa, the same pressure corresponding to the abrupt band gap drop. The SHG intensity of the released sample is the same as the initial one (Figure S2), which indicates a reversible variation.

To further analyze the relationship between crystal symmetry and SHG properties, the polarization-resolved SHG measurements at different pressures were performed in a parallel configuration (Figure S3). CIPS possesses a two-lobe pattern under ambient conditions, which is consistent with point groups  $C_s$  crystal as reported before.<sup>44</sup> As pressure increases to 4.6 GPa, the two-lobe shape remains, which demonstrates the same crystallographic space groups in CIPS before 5 GPa (Figure S3). The polarization-resolved SHG measurements indicate that such an enhanced SHG response in CIPS is attributed to the evolution of local structures. In addition, the excitation power dependence of the SHG peak intensity in logarithmic coordinates is shown in Figure 1e. The fitting slope shows no saturation and hysteresis behavior and is close to the theoretical value of 2, agreeing well with features of the second-order NLO process (Figure 1f).<sup>37</sup>

**Pressure-Induced Cationic Displacement and Phase Transition.** The enhanced SHG is believed to be correlated to the pressure-driven evolution of the local structure. To investigate the structural variations, *in situ* synchrotron X-ray

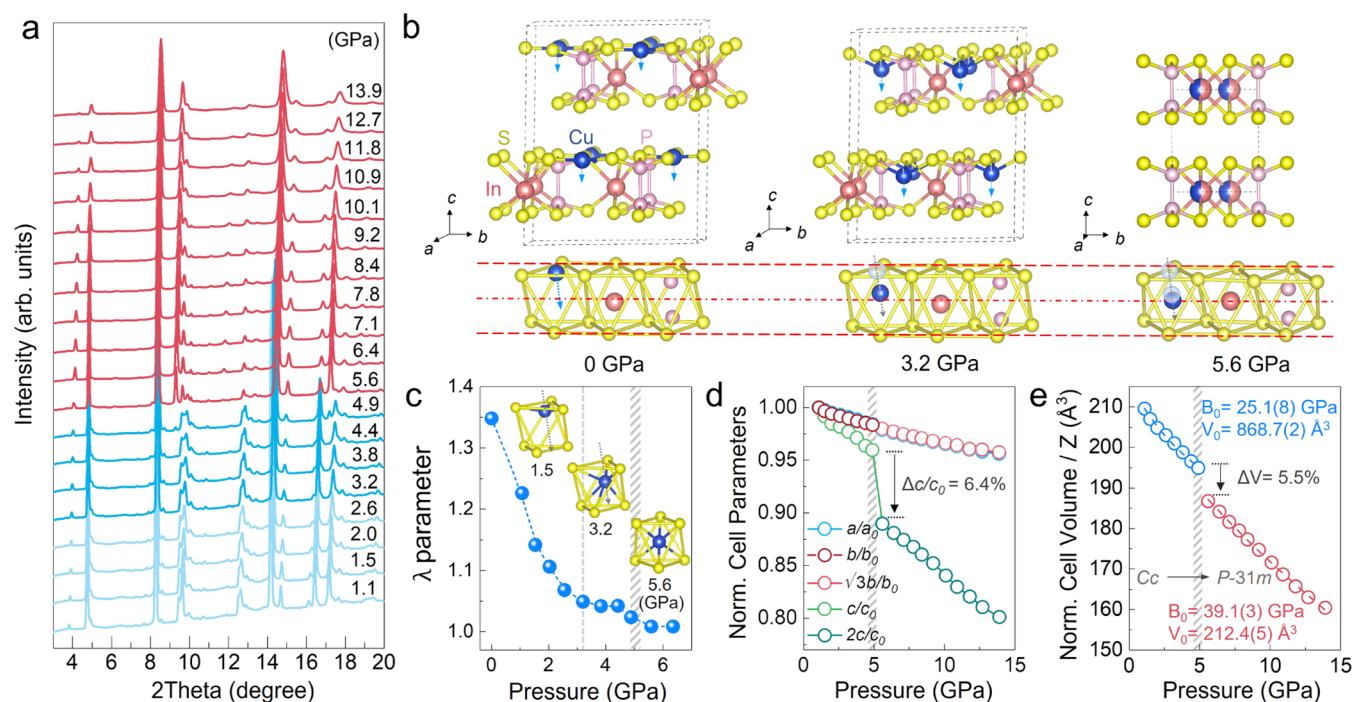


**Figure 2.** Pressure-induced structural variations of CIPS. (a) Synchrotron XRD patterns of CIPS at selected pressures. New peaks emerge at 5.6 GPa, which suggests a pressure-induced phase transition. (b) Crystal structures of CIPS at selected pressures. The Cu cations move from the vdW edge to the octahedral cages. (c) Pressure-dependent variations of the quadratic elongation parameters  $\lambda$ , where  $\lambda$  describes the degree of Cu off-centering distortions in the octahedra. (d) Cell parameters and (e) unit cell volume as a function of pressure. The volume collapses ( $\Delta V = 5.5\%$ ) after the phase transition are owing to the abrupt shrinkage of the  $c$  axis ( $\Delta c/c_0 = 6.4\%$ ). The values of bulk modulus  $B_0$  were determined to be 25.1(8) and 39.1(3) GPa in the monoclinic ( $Cc$ ) and trigonal ( $P\bar{3}1m$ ) phases, respectively.

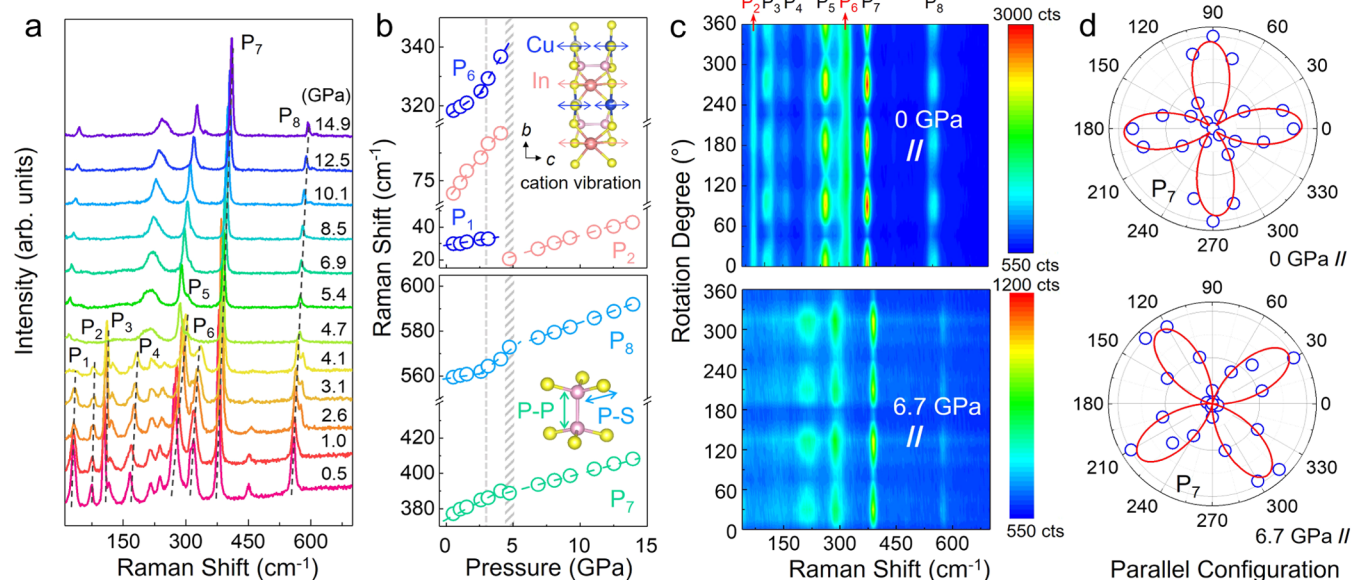


**Figure 3.** Variations of local structure and phonon vibrational anisotropy of CIPS under pressure. (a) *In situ* Raman spectra of CIPS at selected pressures. (b) Pressure dependence of the Raman-active modes of the  $[P_2S_6]$  framework and cation vibrations. (c) False-color plot of polarized Raman intensities of CIPS measured in parallel polarization configurations at 0 and 6.7 GPa. (d) Normalized Raman polar plots of the  $P_7$  peak at 0 and 6.7 GPa. The red lines are the fits using the complex Raman tensors (details in the Supporting Information).

diffraction (XRD) was conducted under high pressures (Figures 2a, and S4 and Table S1). As pressure increases, all Bragg diffraction peaks shift to higher two-theta angles due to the lattice contraction. When the applied pressure reaches 5.6 GPa, some of the peaks weaken and new peaks emerge, implying the occurrence of a phase transition (Figure 2a). It

was reported that CIPS possesses a typical 2D layered structure of  $Cc$  noncentrosymmetry under ambient conditions.<sup>21</sup> Each layer contains a sulfur framework with the octahedral cages filled by a void, In, and P–P units (left panel of Figure 2b).<sup>15,21</sup> Cu exists in the edge of the unfilled sulfur octahedron. After the pressure-induced phase transition, the

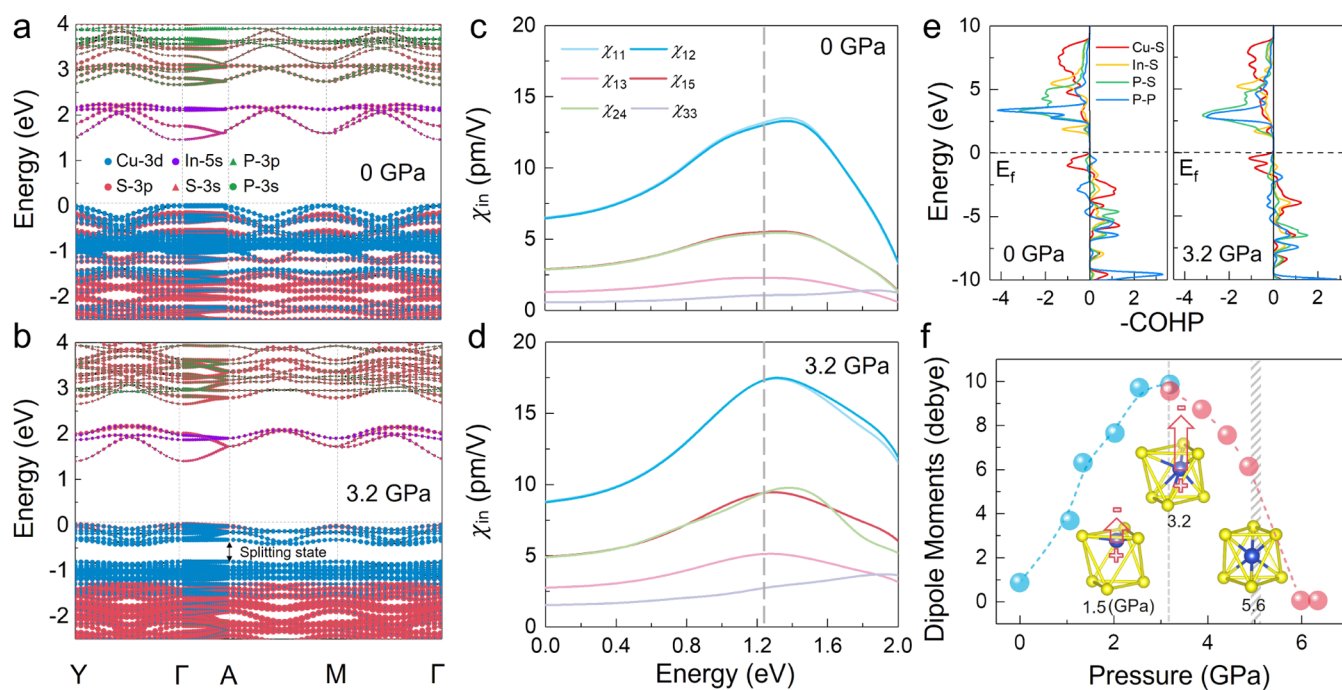


**Figure 4.** Theoretical calculation results and the origin of enhanced SHG. The calculated electronic structures of CIPS at (a) ambient pressure and (b) 3.2 GPa. Frequency-dependent second-order susceptibilities ( $\chi_{in}$ ) at (c) 0 and (d) 3.2 GPa. (e) COHP curves at 0 and 3.2 GPa. (f) Pressure-dependent variations of the dipole moment ( $\mu$ ). With the increase of  $\mu$  value, the SHG response strengthens.

trigonal  $P\bar{3}1m$  centrosymmetric structure was determined by analyzing high-pressure single-crystal XRD (Table S2), where the  $S_6$  octahedral cages are respectively occupied by Cu/In and P–P units (right panel of Figure 2b). The slip of layers in CIPS during compression leads to the mixed site occupation of Cu/In atoms and the lower deformation of the  $[P_2S_6]$  framework after the phase transition is attributed to the strong covalent bonding of P–P and P–S.<sup>15,45</sup> Comparing these two structures, one can see a noticeable change in the coordination environment of Cu (Figure 2b and Table S3). Such an obviously different local structure suggests that there exists a dynamic displacement of Cu cations from the vdW edge to the octahedral cage during compression. Notably, the displacement of Cu cations modulates the octahedral distortion, which can affect local polarization and SHG response. To describe the degree of such structural distortion, we introduce the octahedral quadratic elongation parameter ( $\lambda$ ).<sup>34</sup> The  $\lambda$  value is 1.35 under ambient conditions, where Cu is located in the edge of sulfur octahedra (Figure 2c). With the migration of Cu cations, the  $\lambda$  value decreases to 1.05 at 3.2 GPa. Meanwhile, the resulting  $[CuS_6]$  octahedra exhibit an off-centering distortion, which contributes to the enhanced SHG response. The  $\lambda$  value further decreases to 1 after the phase transition over 5.6 GPa, indicating that the off-centering distortion is suppressed with no SHG response that can be detected.

The pressure-induced variations of lattice parameters and unit cell volume are shown in Figure 2d,e, and Table S1. The monoclinic phase shows large anisotropic compressibility, where the  $c$  axis shortens more rapidly than the  $a$  and  $b$  axes (Figure 2d). Such anisotropic compressibility can cause swing-like Cu vibration in the  $[CuS_3]$  trigonal plane, which is favorable to Cu cationic migration.<sup>46,47</sup> Thus, when applying pressure, Cu plays strong out-of-plane vibration along the  $c$  direction and subsequently moves away from the vdW edge to the octahedral cage (Figure 2b). Figure 2e shows a dramatic

reduction of unit cell volume after the phase transition ( $\Delta V = 5.5\%$ ), which is consistent with the abrupt shrinkage of the  $c$  axis ( $\Delta c/c_0 = 6.4\%$ ). The phenomenon suggests that the volume collapse is mainly attributed to the moveable Cu cations, which fill up octahedral voids and lead to denser layers. The values of bulk modulus  $B_0$  were 25.1(8) and 39.1(3) GPa before and after the phase transition, respectively.<sup>33</sup>

**Local Structure Evolution and Anisotropic Vibration under Pressure.** To further elucidate the behavior of the Cu cation displacement and its interplay with the framework, we examined the evolution of local structures by employing *in situ* Raman spectroscopy (Figures 3a,b, S5 and S6). The  $P_1$ ,  $P_2$ , and  $P_6$  modes are associated with cationic vibrations. Thereinto, the  $P_1$  mode is identified as the out-of-plane vibration of Cu (Figures 3b and S5).<sup>48,49</sup> It disappears over 3.1 GPa, suggesting the considerable changes in the vibration and coordination environment of Cu (Figure 3b). Such a change is consistent with the XRD results, which confirm the change of the coordination environment from the  $[CuS_3]$  trigonal plane to  $[CuS_6]$  octahedra. The  $P_2$  and  $P_6$  modes are assigned to the asymmetric stretching vibration of In–S and Cu–S bonding, respectively, which presents an off-centering position in the octahedral  $S_6$  cage.<sup>48,49</sup> The disappearance of these peaks ( $P_2$  and  $P_6$  modes) after the phase transition indicates a regular octahedral coordination (Figure 3b). On the other hand, the bending and stretching vibration modes of the  $[P_2S_6]$  framework are related to the Raman peaks of  $P_4$ ,  $P_5$ ,  $P_7$ , and  $P_8$  (Figures 3b and S6).<sup>48,49</sup> The  $P_3$  mode corresponds to anion deformation, which is closely relevant to distortions of the  $S_6$  cage.<sup>48</sup> The dramatic variations of  $P_3$ ,  $P_4$ , and  $P_5$  modes take place at 5.4 GPa, owing to the noncentrosymmetric-to-centrosymmetric phase transition, whereas the  $P_7$  and  $P_8$  modes remain after the phase transition, which confirms a rigid  $[P_2S_6]$  framework in CIPS. Upon decompression, the Raman modes of the released CIPS are the same as those

under ambient conditions (Figure S7), which indicates a reversible phase transition during the compression–decompression cycle.

Due to the noncentrosymmetric space group  $Cc$ , the phonon vibration of CIPS is anisotropic before the phase transition. ARPERS was performed to investigate the phonon vibrational anisotropy. Under ambient conditions,  $P_2$  and  $P_6$  modes demonstrate  $A'$ -like vibrations and show weak 4- and 2-fold periodic patterns in parallel and perpendicular polarization configurations, respectively, while the other Raman modes demonstrate  $A''$ -like vibrations and exhibit 4-fold patterns in both polarization configurations (Figures 3c and S8). The ARPERS results show two different types of anisotropic vibration in CIPS, where cations tend to vibrate out of the  $ab$  plane ( $A'$  mode) but the framework is likely to vibrate within the  $ab$  plane ( $A''$  mode).<sup>44</sup> Thus, taken together with swing-like Cu vibration in  $[CuS_3]$ , it is no doubt that Cu cations are much easier to migrate out of the  $ab$  plane under pressure. As the pressure reaches 6.7 GPa, all peaks in the  $P\bar{3}1m$  space group show 4-fold patterns in both parallel and perpendicular polarization configurations (Figures 3c and S8). To explain these polarization configurations, the intensity of the Raman signal can be expressed as the equation  $I \propto |e_i \mathbf{R} e_j|^2$ .<sup>36,37</sup> Figures 3d and S9 show the polar plot of the  $P_7$  Raman position in parallel and perpendicular polarization configurations (details in the Supporting Information). The fitting results confirm that CIPS belongs to the  $C_s$  point group under room conditions and the  $D_{3d}$  point group at high pressure. The phase transition leads to the disappearance of out-of-plane vibrational modes of cations (Figure 3c), indicating isotropic vibration of cations and framework in CIPS under high pressure.

**Theoretical Calculations and the Origin of Enhanced SHG.** By analyzing the NLO performance and local structure of CIPS, we have demonstrated the effects of Cu cationic displacement on SHG response. To get more insights into a comprehensive cognition of the relationships between these local structures and optical nonlinearity, we investigated the SHG properties of CIPS using first-principles calculation. The electronic band structures show that both valance band maximum (VBM) and conduction band minimum (CBM) are located at  $\Gamma$  point (Figure 4a,b), indicating that CIPS is a direct band gap semiconductor. VBM is mainly composed of S 3p and Cu 3d states, while S 3p and In 5s contribute to CBM. The splitting of Cu–S states at 3.2 GPa is owing to the off-centering distortion of  $[CuS_6]$  octahedra, which eliminates band degeneracies below the VB band.<sup>50</sup> The calculated frequency-dependent second-order susceptibilities ( $\chi_{in}$ ) are shown in Figure 4c,d. CIPS belongs to the  $C_s$  point group with six nonvanishing second-order susceptibility tensors under Kleinman symmetry ( $\chi_{11}$ ,  $\chi_{12}$ ,  $\chi_{13}$ ,  $\chi_{15}$ ,  $\chi_{24}$ , and  $\chi_{33}$ ).<sup>51</sup> Under ambient conditions, the six independent second-order tensors are 13.2, 13.0, 2.3, 5.5, 5.5, and 1.1 pm/V at the excitation wavelength of 1030 nm (1.24 eV). They increase to 17.3, 17.3, 5.1, 9.5, 9.5, and 2.7 pm/V at 3.2 GPa, indicating a stronger SHG response. Such a result confirms that the contributions of cationic displacement on octahedral distortion enhance the SHG response.

To get a deeper understanding of the origin of the enhanced SHG response, we calculated the crystal orbital Hamilton population (COHP) and dipole moments ( $\mu$ ).<sup>52–55</sup> The analysis of COHP curves reveals that the antibonding states of Cu–S are mainly dominated in the valence bands near the

Fermi level (Figure 4e). The hybridization between Cu and S around the Fermi level means a strong interband dipole and a high possibility of quantum transition between valence and conducting bands, which is beneficial to the SHG response. The  $\mu$  values of Cu–S units at different pressures are shown in Figure 4f. The Cu–S bonds (3.08 Å at 3.2 GPa) are longer than the sum of the Shannon crystal radii for a six-coordinated  $Cu^+$  (0.91 Å) and  $S^{2-}$  (1.70 Å) but shorter than the corresponding vdW distance of 3.20 Å, and should be taken as an indicative of weak bonding interactions.<sup>56,57</sup> Cu coordination changes from the  $CuS_3$  trigonal plane to  $[CuS_6]$  octahedra at 3.2 GPa. The  $\mu$  value is 0.84 Debye under ambient conditions. As pressure increases to 3.2 GPa,  $\mu$  in both coordination shows larger values than that under ambient pressure, indicating a stronger local polarization caused by the Cu displacement. Such an increased local polarization contributes to the enhancement of SHG response. Above 3.2 GPa, pressure pushes the Cu atoms toward the center of the  $[CuS_6]$  octahedron, forming less distorted octahedra. This process reduces the dipole moment and weakens the local polarization, resulting in a considerable decrease of SHG.

## CONCLUSIONS

In conclusion, using pressure to regulate the cationic configuration, we have achieved a 10-fold boost of SHG response in a vdW  $CuInP_2S_6$  crystal. Both *in situ* synchrotron XRD and polarized Raman spectroscopy indicate the anisotropic compression of CIPS, which leads to Cu cationic displacement from the vdW edge to the octahedral cage. This process generates highly distorted  $[CuS_6]$  octahedra at 3.2 GPa, giving rise to the significant enhancement of SHG. The distortion is suppressed under further compression and finally results in a  $Cc$  to  $P\bar{3}1m$  phase transition, corresponding to the weakening and eventual disappearance of SHG. In combination with first-principles calculations, the contributions of Cu cationic displacement on the octahedral distortion and interband dipole moments were quantitatively demonstrated. The distorted local structure formed by cationic displacement gives strong polarization and a high dipole moment, determining the enhanced SHG. Our work demonstrates the significant contributions of cationic configuration in NLO materials, which have long been underappreciated. The findings presented here open a new pathway to design and optimize advanced NLO materials by modifying the local structures from the point of view of cationic configurations using the methods, such as chemical tailoring (*e.g.*, cationic doping), interfacial engineering, and straining engineering.

## ASSOCIATED CONTENT

### Supporting Information

The Supporting Information is available free of charge at <https://pubs.acs.org/doi/10.1021/acs.chemmater.2c03066>.

Experimental details; polarization dependence of SHG intensity; crystallographic data; Rietveld refinements; Raman spectra; and polarized Raman spectra (PDF)

### Accession Codes

CCDC 2218837 and 2219592 contain supplementary crystallographic data for this paper. These data can be obtained free of charge via [www.ccdc.cam.ac.uk/data\\_request/cif](http://www.ccdc.cam.ac.uk/data_request/cif), or by emailing [data\\_request@ccdc.cam.ac.uk](mailto:data_request@ccdc.cam.ac.uk), or by contacting The Cambridge Crystallographic Data Centre,

12 Union Road, Cambridge CB2 1EZ, U.K.; fax: +44 1223 336033

## AUTHOR INFORMATION

### Corresponding Author

**Xujie Lü** – Center for High Pressure Science and Technology Advanced Research (HPSTAR), Shanghai 201203, P. R. China; [orcid.org/0000-0001-8402-7160](https://orcid.org/0000-0001-8402-7160); Email: [xujie.lu@hpstar.ac.cn](mailto:xujie.lu@hpstar.ac.cn)

### Authors

**Kejun Bu** – Center for High Pressure Science and Technology Advanced Research (HPSTAR), Shanghai 201203, P. R. China; [orcid.org/0000-0002-1466-2764](https://orcid.org/0000-0002-1466-2764)

**Tonghuan Fu** – Center for High Pressure Science and Technology Advanced Research (HPSTAR), Shanghai 201203, P. R. China

**Ziwan Du** – State Key Laboratory of New Ceramics and Fine Processing, School of Materials Science and Engineering, Tsinghua University, Beijing 100084, P. R. China

**Xin Feng** – State Key Laboratory of Materials Processing and Die & Mould Technology School of Materials Science and Engineering, Huazhong University of Science and Technology (HUST), Wuhan 430074, P. R. China

**Dong Wang** – Center for High Pressure Science and Technology Advanced Research (HPSTAR), Shanghai 201203, P. R. China; [orcid.org/0000-0001-5004-9732](https://orcid.org/0000-0001-5004-9732)

**Zhongyang Li** – Center for High Pressure Science and Technology Advanced Research (HPSTAR), Shanghai 201203, P. R. China

**Songhao Guo** – Center for High Pressure Science and Technology Advanced Research (HPSTAR), Shanghai 201203, P. R. China; [orcid.org/0000-0003-0570-0164](https://orcid.org/0000-0003-0570-0164)

**Zongdong Sun** – State Key Laboratory of Materials Processing and Die & Mould Technology School of Materials Science and Engineering, Huazhong University of Science and Technology (HUST), Wuhan 430074, P. R. China

**Hui Luo** – Center for High Pressure Science and Technology Advanced Research (HPSTAR), Shanghai 201203, P. R. China

**Gang Liu** – Center for High Pressure Science and Technology Advanced Research (HPSTAR), Shanghai 201203, P. R. China

**Yang Ding** – Center for High Pressure Science and Technology Advanced Research (HPSTAR), Shanghai 201203, P. R. China

**Tianyou Zhai** – State Key Laboratory of Materials Processing and Die & Mould Technology School of Materials Science and Engineering, Huazhong University of Science and Technology (HUST), Wuhan 430074, P. R. China; [orcid.org/0000-0003-0985-4806](https://orcid.org/0000-0003-0985-4806)

**Qian Li** – State Key Laboratory of New Ceramics and Fine Processing, School of Materials Science and Engineering, Tsinghua University, Beijing 100084, P. R. China; [orcid.org/0000-0001-7922-598X](https://orcid.org/0000-0001-7922-598X)

Complete contact information is available at:

<https://pubs.acs.org/10.1021/acs.chemmater.2c03066>

### Author Contributions

<sup>||</sup>K.B. and T.F. contributed equally to this work. This manuscript was written through contributions of all authors. All authors have given approval to the final version of the manuscript

## Notes

The authors declare no competing financial interest.

## ACKNOWLEDGMENTS

This work was supported by the National Nature Science Foundation of China (NSFC) (Grant Nos. U1930401, U1530402, and 52073155). Portions of this work were performed at Sector 13 (GeoSoilEnviroCARS, The University of Chicago), Advanced Photon Source (APS), Argonne National Laboratory. GeoSoilEnviroCARS was supported by the National Science Foundation-Earth Sciences (EAR-1634415) and Department of Energy-GeoSciences (DE-FG02-94ER14466) and partially by COMPRES under NSF Cooperative Agreement EAR-1606856. This research used resources of the Advanced Photon Source, a U.S. Department of Energy (DOE) Office of Science User Facility, operated for the DOE Office of Science by Argonne National Laboratory under Contract No. DE-AC02-06CH11357.

## REFERENCES

- (1) Ghimire, S.; Reis, D. A. High-harmonic generation from solids. *Nat. Phys.* **2019**, *15*, 10–16.
- (2) Reshef, O.; De Leon, I.; Alam, M. Z.; Boyd, R. W. Nonlinear optical effects in epsilon-near-zero media. *Nat. Rev. Mater.* **2019**, *4*, 535–551.
- (3) Chen, J.; Hu, C.-L.; Kong, F.; Mao, J.-G. High-Performance Second-Harmonic-Generation (SHG) Materials: New Developments and New Strategies. *Acc. Chem. Res.* **2021**, *54*, 2775–2783.
- (4) Khan, A. R.; Zhang, L.; Ishfaq, K.; Ikram, A.; Yildirim, T.; Liu, B.; Rahman, S.; Lu, Y. Optical Harmonic Generation in 2D Materials. *Adv. Funct. Mater.* **2022**, *32*, No. 2105259.
- (5) Becker, P. Borate Materials in Nonlinear Optics. *Adv. Mater.* **1998**, *10*, 979–992.
- (6) Huang, H.; Yao, J.; Lin, Z.; Wang, X.; He, R.; Yao, W.; Zhai, N.; Chen, C.  $\text{NaSr}_3\text{Be}_3\text{B}_3\text{O}_9\text{F}_4$ : A Promising Deep-Ultraviolet Nonlinear Optical Material Resulting from the Cooperative Alignment of the  $[\text{Be}_3\text{B}_3\text{O}_{12}\text{F}]^{10-}$  Anionic Group. *Angew. Chem., Int. Ed.* **2011**, *50*, 9141–9144.
- (7) Lin, K.; Gong, P.; Chu, S.; Li, Q.; Lin, Z.; Wu, H.; Wang, Q.; Wang, J.; Kim, M. J.; Kato, K.; Wang, C.-W.; Liu, X.; Huang, Q.; Chen, J.; Zhu, H.; Deng, J.; Xing, X. Strong Second Harmonic Generation in a Tungsten Bronze Oxide by Enhancing Local Structural Distortion. *J. Am. Chem. Soc.* **2020**, *142*, 7480–7486.
- (8) Cammarata, A.; Rondinelli, J. M. Contributions of Correlated Acentric Atomic Displacements to the Nonlinear Second Harmonic Generation and Response. *ACS Photonics* **2014**, *1*, 96–100.
- (9) Ra, H.-S.; Ok, K. M.; Halasyamani, P. S. Combining Second-Order Jahn–Teller Distorted Cations to Create Highly Efficient SHG Materials: Synthesis, Characterization, and NLO Properties of  $\text{BaTeM}_2\text{O}_9$  (M =  $\text{Mo}^{6+}$  or  $\text{W}^{6+}$ ). *J. Am. Chem. Soc.* **2003**, *125*, 7764–7765.
- (10) Liu, Y.; Gong, Y.-P.; Geng, S.; Feng, M.-L.; Manidaki, D.; Deng, Z.; Stoumpos, C. C.; Canepa, P.; Xiao, Z.; Zhang, W.-X.; Mao, L. Hybrid Germanium Bromide Perovskites with Tunable Second Harmonic Generation. *Angew. Chem., Int. Ed.* **2022**, *61*, No. e202208875.
- (11) Yang, Y.; Chu, Y.; Zhang, B.; Wu, K.; Pan, S. Unique Unilateral-Chelated Mode-Induced d–p– $\pi$  Interaction Enhances Second-Harmonic Generation Response in New  $\text{Ln}_3\text{LiMS}_7$  Family. *Chem. Mater.* **2021**, *33*, 4225–4230.
- (12) Liu, B.-W.; Hu, C.-L.; Zeng, H.-Y.; Jiang, X.-M.; Guo, G.-C. Strong SHG Response via High Orientation of Tetrahedral Functional Motifs in Polyselenide  $\text{A}_2\text{Ge}_4\text{Se}_{10}$  (A = Rb, Cs). *Adv. Opt. Mater.* **2018**, *6*, No. 1800156.
- (13) Ran, M.-Y.; Ma, Z.; Chen, H.; Li, B.; Wu, X.-T.; Lin, H.; Zhu, Q.-L. Partial Isovalent Anion Substitution to Access Remarkable Second-Harmonic Generation Response: A Generic and Effective

Strategy for Design of Infrared Nonlinear Optical Materials. *Chem. Mater.* **2020**, *32*, 5890–5896.

(14) Wang, R.; Liang, F.; Wang, F.; Guo, Y.; Zhang, X.; Xiao, Y.; Bu, K.; Lin, Z.; Yao, J.; Zhai, T.; Fuqiang, H.  $\text{Sr}_6\text{Cd}_2\text{Sb}_6\text{O}_{710}$ : Strong SHG response activated by highly polarizable Sb/O/S groups. *Angew. Chem.* **2019**, *131*, 8162–8165.

(15) Susner, M. A.; Chyasnachyus, M.; McGuire, M. A.; Ganesh, P.; Maksymovych, P. Metal Thio- and Selenophosphates as Multifunctional van der Waals Layered Materials. *Adv. Mater.* **2017**, *29*, No. 1602852.

(16) Kang, L.; Zhou, M.; Yao, J.; Lin, Z.; Wu, Y.; Chen, C. Metal Thiophosphates with Good Mid-infrared Nonlinear Optical Performances: A First-Principles Prediction and Analysis. *J. Am. Chem. Soc.* **2015**, *137*, 13049–13059.

(17) Rahman, S.; Yildirim, T.; Tebyetekerwa, M.; Khan, A. R.; Lu, Y. Extraordinary Nonlinear Optical Interaction from Strained Nanostructures in van der Waals  $\text{CuInP}_2\text{S}_6$ . *ACS Nano* **2022**, *16*, 13959–13968.

(18) Brehm, J. A.; Neumayer, S. M.; Tao, L.; O'Hara, A.; Chyasnachyus, M.; Susner, M. A.; McGuire, M. A.; Kalinin, S. V.; Jesse, S.; Ganesh, P.; Pantelides, S. T.; Maksymovych, P.; Balke, N. Tunable quadruple-well ferroelectric van der Waals crystals. *Nat. Mater.* **2020**, *19*, 43–48.

(19) Zhang, D.; Luo, Z.-D.; Yao, Y.; Schoenherr, P.; Sha, C.; Pan, Y.; Sharma, P.; Alexe, M.; Seidel, J. Anisotropic Ion Migration and Electronic Conduction in van der Waals Ferroelectric  $\text{CuInP}_2\text{S}_6$ . *Nano Lett.* **2021**, *21*, 995–1002.

(20) Ma, R.-R.; Xu, D.-D.; Zhong, Q.-L.; Zhong, C.-R.; Huang, R.; Xiang, P.-H.; Zhong, N.; Duan, C.-G. Nanoscale Mapping of Cu-Ion Transport in van der Waals Layered  $\text{CuCrP}_2\text{S}_6$ . *Adv. Mater. Interfaces* **2022**, *9*, No. 2101769.

(21) Liu, F.; You, L.; Seyler, K. L.; Li, X.; Yu, P.; Lin, J.; Wang, X.; Zhou, J.; Wang, H.; He, H.; Pantelides, S. T.; Zhou, W.; Sharma, P.; Xu, X.; Ajayan, P. M.; Wang, J.; Liu, Z. Room-temperature ferroelectricity in  $\text{CuInP}_2\text{S}_6$  ultrathin flakes. *Nat. Commun.* **2016**, *7*, No. 12357.

(22) Bu, K.; Hu, Q.; Qi, X.; Wang, D.; Guo, S.; Luo, H.; Lin, T.; Guo, X.; Zeng, Q.; Ding, Y.; Huang, F.; Yang, W.; Mao, H.-K.; Lü, X. Nested order-disorder framework containing a crystalline matrix with self-filled amorphous-like innards. *Nat. Commun.* **2022**, *13*, No. 4650.

(23) Guo, S.; Bu, K.; Li, J.; Hu, Q.; Luo, H.; He, Y.; Wu, Y.; Zhang, D.; Zhao, Y.; Yang, W.; Kanatzidis, M.; Lü, X. Enhanced Photocurrent of All-Inorganic Two-Dimensional Perovskite  $\text{Cs}_2\text{PbI}_2\text{Cl}_2$  via Pressure-Regulated Excitonic Features. *J. Am. Chem. Soc.* **2021**, *143*, 2545–2551.

(24) Lü, X.; Stoumpos, C.; Hu, Q.; Ma, X.; Zhang, D.; Guo, S.; Hoffman, J.; Bu, K.; Guo, X.; Wang, Y.; Ji, C.; Chen, H.; Xu, H.; Jia, Q.; Yang, W.; Kanatzidis, M. G.; Mao, H.-K. Regulating off-centering distortion maximizes photoluminescence in halide perovskites. *Nat. Sci. Rev.* **2021**, *8*, No. nwa288.

(25) Shi, Y.; Ma, Z.; Zhao, D.; Chen, Y.; Cao, Y.; Wang, K.; Xiao, G.; Zou, B. Pressure-Induced Emission (PIE) of One-Dimensional Organic Tin Bromide Perovskites. *J. Am. Chem. Soc.* **2019**, *141*, 6504–6508.

(26) Navrotsky, A. Pressure-induced structural changes cause large enhancement of photoluminescence in halide perovskites: a quantitative relationship. *Nat. Sci. Rev.* **2021**, *8*, No. nwa041.

(27) Guo, S.; Li, Y.; Mao, Y.; Tao, W.; Bu, K.; Fu, T.; Zhao, C.; Luo, H.; Hu, Q.; Zhu, H.; Shi, E.; Yang, W.; Dou, L.; Lü, X. Reconfiguring band-edge states and charge distribution of organic semiconductor-incorporated 2D perovskites via pressure gating. *Sci. Adv.* **1984**, *8*, No. eadd1984.

(28) Mao, H. K.; Xu, J.; Bell, P. Calibration of the ruby pressure gauge to 800 kbar under quasi-hydrostatic conditions. *J. Geophys. Res.* **1986**, *91*, 4673–4676.

(29) Chen, X.; Lou, H.; Zeng, Z.; Cheng, B.; Zhang, X.; Liu, Y.; Xu, D.; Yang, K.; Zeng, Q. Structural transitions of 4: 1 methanol–ethanol mixture and silicone oil under high pressure. *Matter Radiat. Extremes* **2021**, *6*, No. 038402.

(30) Prescher, C.; Prakapenka, V. B. DIOPTAS: a program for reduction of two-dimensional X-ray diffraction data and data exploration. *High Pressure Res.* **2015**, *35*, 223–230.

(31) Rodríguez-Carvajal, J. FullProf.CEA/Saclay2001.

(32) Sheldrick, G. M. Crystal structure refinement with SHELXL. *Acta Crystallogr., Sect. C: Struct. Chem.* **2015**, *71*, 3–8.

(33) Katsura, T.; Tange, Y. A Simple Derivation of the Birch–Murnaghan Equations of State (EOSs) and Comparison with EOSs Derived from Other Definitions of Finite Strain. *Minerals* **2019**, *9*, No. 745.

(34) Robinson, K.; Gibbs, G. V.; Ribbe, P. H. Quadratic Elongation: A Quantitative Measure of Distortion in Coordination Polyhedra. *Science* **1971**, *172*, 567–570.

(35) Kortüm, G.; Braun, W.; Herzog, G. Principles and techniques of diffuse-reflectance spectroscopy. *Angew. Chem., Int. Ed.* **1963**, *2*, 333–341.

(36) Peter, Y.; Cardona, M. *Fundamentals of Semiconductors: Physics and Materials Properties*; Springer Science & Business Media, 2010; p 378.

(37) Fang, Y.; Wang, F.; Wang, R.; Zhai, T.; Huang, F. 2D  $\text{NbOI}_2$ : A Chiral Semiconductor with Highly In-Plane Anisotropic Electrical and Optical Properties. *Adv. Mater.* **2021**, *33*, No. 2101505.

(38) Perdew, J. P.; Burke, K.; Ernzerhof, M. Generalized gradient approximation made simple. *Phys. Rev. Lett.* **1996**, *77*, 3865–3868.

(39) Kresse, G.; Furthmüller, J. Efficient iterative schemes for ab initio total-energy calculations using a plane-wave basis set. *Phys. Rev. B* **1996**, *54*, 11169–11186.

(40) Bassani, F.; Parravicini, G. *Electronic States and Optical Transitions in Solids*; Pergamon Press, Oxford, 1975; p 58.

(41) Gajdoš, M.; Hummer, K.; Kresse, G.; Furthmüller, J.; Bechstedt, F. Linear optical properties in the projector-augmented wave methodology. *Phys. Rev. B* **2006**, *73*, No. 045112.

(42) Boyd, R. *Nonlinear Optics*; Academic Press: New York, 2003; p 25.

(43) Ma, R.-R.; Xu, D.-D.; Guan, Z.; Deng, X.; Yue, F.; Huang, R.; Chen, Y.; Zhong, N.; Xiang, P.-H.; Duan, C.-G. High-speed ultraviolet photodetectors based on 2D layered  $\text{CuInP}_2\text{S}_6$  nanoflakes. *Appl. Phys. Lett.* **2020**, *117*, No. 131102.

(44) Beams, R.; Caňgado, L. G.; Krylyuk, S.; Kalish, I.; Kalanyan, B.; Singh, A. K.; Choudhary, K.; Bruma, A.; Vora, P. M.; Tavazza, F.; Davydov, A. V.; Stranick, S. J. Characterization of Few-Layer 1T'  $\text{MoTe}_2$  by Polarization-Resolved Second Harmonic Generation and Raman Scattering. *ACS Nano* **2016**, *10*, 9626–9636.

(45) Li, Z.; Yao, J.; Wu, Y. Chalcophosphates: A Treasure House of Infrared Nonlinear Optical Materials. *Cryst. Growth Des.* **2020**, *20*, 7550–7564.

(46) Qiu, W.; Xi, L.; Wei, P.; Ke, X.; Yang, J.; Zhang, W. Part-crystalline part-liquid state and rattling-like thermal damping in materials with chemical-bond hierarchy. *Proc. Natl. Acad. Sci. U.S.A.* **2014**, *111*, 15031–15035.

(47) Suekuni, K.; Lee, C. H.; Tanaka, H. I.; Nishibori, E.; Nakamura, A.; Kasai, H.; Mori, H.; Usui, H.; Ochi, M.; Hasegawa, T.; Nakamura, M.; Ohira-Kawamura, S.; Kikuchi, T.; Kaneko, K.; Nishiate, H.; Hashikuni, K.; Kosaka, Y.; Kuroki, K.; Takabatake, T. Retreat from Stress: Rattling in a Planar Coordination. *Adv. Mater.* **2018**, *30*, No. 1706230.

(48) Vysochanskii, Y. M.; Stephanovich, V. A.; Molnar, A. A.; Cajipe, V. B.; Bourdon, X. Raman spectroscopy study of the ferroelectric-paraelectric transition in layered  $\text{CuInP}_2\text{S}_6$ . *Phys. Rev. B* **1998**, *58*, 9119–9124.

(49) Neal, S. N.; Singh, S.; Fang, X.; Won, C.; Huang, F.-t.; Cheong, S.-W.; Rabe, K. M.; Vanderbilt, D.; Musfeldt, J. L. Vibrational properties of  $\text{CuInP}_2\text{S}_6$  across the ferroelectric transition. *Phys. Rev. B* **2022**, *105*, No. 075151.

(50) Akopov, G.; Viswanathan, G.; Hewage, N. W.; Yox, P.; Wu, K.; Kovnir, K. Pd and octahedra do not get along: Square planar  $[\text{PdS}_4]$  units in non-centrosymmetric  $\text{La}_6\text{PdSi}_2\text{S}_{14}$ . *J. Alloys Compd.* **2022**, *902*, No. 163756.

(51) Zhang, M.-J.; Jiang, X.-M.; Zhou, L.-J.; Guo, G.-C. Two phases of Ga<sub>2</sub>S<sub>3</sub>: promising infrared second-order nonlinear optical materials with very high laser induced damage thresholds. *J. Mater. Chem. C* **2013**, *1*, 4754–4760.

(52) Deringer, V. L.; Tchougréeff, A. L.; Dronskowski, R. Crystal Orbital Hamilton Population (COHP) Analysis As Projected from Plane-Wave Basis Sets. *J. Phys. Chem. A* **2011**, *115*, 5461–5466.

(53) Lin, H.; Chen, L.; Yu, J.-S.; Chen, H.; Wu, L.-M. Infrared SHG Materials CsM<sub>3</sub>Se<sub>6</sub> (M = Ga/Sn, In/Sn): Phase Matchability Controlled by Dipole Moment of the Asymmetric Building Unit. *Chem. Mater.* **2017**, *29*, 499–503.

(54) Sivakumar, T.; Chang, H. Y.; Baek, J.; Halasyamani, P. S. Two New Noncentrosymmetric Polar Oxides: Synthesis, Characterization, Second-Harmonic Generating, and Pyroelectric Measurements on TlSeVO<sub>5</sub> and TlTeVO<sub>5</sub>. *Chem. Mater.* **2007**, *19*, 4710–4715.

(55) Maggard, P. A.; Nault, T. S.; Stern, C. L.; Poeppelmeier, K. R. Alignment of acentric MoO<sub>3</sub>F<sub>3</sub><sup>3-</sup> anions in a polar material: (Ag<sub>3</sub>MoO<sub>3</sub>F<sub>3</sub>)(Ag<sub>3</sub>MoO<sub>4</sub>)Cl. *J. Solid State Chem.* **2003**, *175*, 27–33.

(56) Baggio, R.; Garland, M. T.; Manzur, J.; Peña, O.; Pereg, M.; Spodine, E.; Vega, A. A dinuclear copper (II) complex involving monoatomic O-carboxylate bridging and Cu–S (thioether) bonds: [Cu(tda)(phen)]<sub>2</sub>·H<sub>2</sub>tda (tda = thiodiacetate, phen = phenanthroline). *Inorg. Chim. Acta* **1999**, *286*, 74–79.

(57) Huheey, J. E. *Principles of Structure and Reactivity*; Harper & Row, 1983; p 64.